



# Cobalt clusters decorated $\text{Co}_x\text{Mn}_{1-x}\text{O}$ nanocomposites for improving the efficiency of syngas to lower olefins with lower $\text{CO}_2$ emission

Shuai Lyu<sup>1</sup>, Qingsen Wu<sup>1</sup>, Zhe Li, Yuhua Zhang, Jinlin Li<sup>\*</sup>, Li Wang<sup>\*</sup>

Key Laboratory of Catalysis and Energy Materials Chemistry of Ministry of Education & Hubei Key Laboratory of Catalysis and Materials Science, South-Central Minzu University, Wuhan 430074, China



## ARTICLE INFO

### Keywords:

Lower olefins  
Fischer-Tropsch synthesis  
Carbon usage  
 $\text{CO}_2$  selectivity  
Co cluster

## ABSTRACT

Fischer-Tropsch synthesis has long been the most important means to convert non-fossil resources to high value-added products, i.e., lower olefins. However, the selectivity tends to be low. In the past decades, the efforts devoted to improving the selectivity toward lower olefins have been rewarded, but the selectivity toward undesired  $\text{CO}_2$  is overlooked and normally over 40%, resulting in a poor carbon usage effectiveness. Here, we describe  $\text{Co}_x\text{Mn}_{1-x}\text{O}$  nanocrystals to achieve a high selectivity (65.4%) toward lower olefins and a remarkably low  $\text{CO}_2$  selectivity of only 13.7%. Such superior performance is due to the formation of stable  $\text{Co}^0$  clusters ( $<1$  nm) as active sites, which facilitate the activation of CO and weaken the C-C coupling to generate lower olefins, and suppress water-gas shift reaction to minimize  $\text{CO}_2$  emission. Our work represents a conceptual advance to the design of highly efficient catalysts for superior lower olefins selectivity by taking  $\text{CO}_2$  into account.

## 1. Introduction

Lower olefins ( $\text{C}_2^{\text{-}}\text{-C}_4^{\text{-}}$ ) are of pivot significance as building blocks in chemical industry for the manufacture of a variety of products. The traditional methods for the production of olefins require the use of naphtha, diesel, and other petroleum products as precursors [1,2]. The growing demands for olefins and dwindling petroleum supplies compel the development of technologies for the generation of olefins from nonpetroleum resources [3]. Fischer-Tropsch synthesis (FTS) represents the most reliable human endeavor to convert syngas, which could be derived from biomass, coal, and natural gas, producing clean fuels and high-value-added chemicals especially lower olefins [4-7]. FTS is essentially a polymerization reaction that takes place on the surface of various catalysts, generating products that follow the traditional Anderson-Schulz-Flory (ASF) distribution featured with low selectivity [8]. In the past decades, there have been numerous studies on breaking the ASF restriction in FTS to render high selectivity towards desired products, for example, lower olefins [9-13].

Recently, notable achievements have been made in selective conversion of syngas towards lower olefins (FTO) through the delicate design of the structures of the catalysts. For example, de Jong and co-workers reported a Fe-based catalyst promoted by sulfur and sodium to

achieve up to 61% selectivity for  $\text{C}_2^{\text{-}}\text{-C}_4^{\text{-}}$  olefins, which is close to the upper limit predicted by the ASF theory [14]. Zhong and coworkers also obtained up to 61% selectivity for lower olefins in syngas conversion through the manipulation of the exposed active facets of  $\text{Co}_2\text{C}$  nanoprisms [15]. Bao and coworkers described a remarkably high selectivity of 80% for lower olefins at 400 °C that breaks the theoretical ASF limit by using OX-ZEO relay catalysts [16]. These efforts are encouraging, however, the calculation of the selectivity in previous studies excludes the fraction of  $\text{CO}_2$ , which normally accounts for around 45% in terms of carbon number and poses great challenges for efficient carbon usage. Very recently, Ding and coworkers reported a variation of the micro-environment of the active iron carbide catalyst by using a hydrophobic shell, which effectively reduced the retention time of water on the catalyst surface and suppressed the water gas shift reaction, resulting in a significant decrease of the  $\text{CO}_2$  selectivity of only around 10% with an olefin yield of 36.6% [17]. It is thus highly desired to achieve both high olefin yield and low  $\text{CO}_2$  selectivity, for the elevation of carbon efficiency in syngas conversion and the contribution to the carbon emission reduction on a global scale.

Previous studies have concluded that the  $\text{Co}_2\text{C}$  nanoprisms generated during the reaction are the active sites for the conversion of syngas to lower olefins, where the presence of Na element facilitates the formation

\* Corresponding authors.

E-mail addresses: [Jinlinli@aliyun.com](mailto:Jinlinli@aliyun.com) (J. Li), [li.wang@scuec.edu.cn](mailto:li.wang@scuec.edu.cn) (L. Wang).

<sup>1</sup> These authors contributed equally to this work.

of  $\text{Co}_2\text{C}$  nanoprisms from  $\text{CoMn}$  oxides catalyst. Nevertheless, the  $\text{Co}_2\text{C}$  phase possesses high water-gas-shift reaction activity, resulting in a high  $\text{CO}_2$  emission in the FTO process. In this study, we report a surface reconstruction strategy to manipulate the catalytic performance of a series of  $\text{CoMn}$  oxides nanocomposite catalysts in FTS. An illustration of the surface reconstruction of  $\text{CoMn}$  oxide nanocomposite to generate  $\text{Co}^0$  clusters during reduction treatment and FTS reaction is presented in Fig. 1. Remarkably, the optimal catalyst achieved high selectivity towards lower olefin (65.4%), and low  $\text{CO}_2$  selectivity of only 13.7%. Several ex-situ characterization techniques reveal that the  $\text{Co}^0$  clusters are the key active sites for such prominent catalytic performance. Theoretical calculations suggest that compared to normal  $\text{Co}$  metal, the  $\text{Co}^0$  clusters are thermodynamically less favored for the formation of  $\text{Co}_2\text{C}$  phase, thus suppressing the  $\text{CO}_2$  formation (Fig. 1). Such surface reconstruction represents an effective strategy to boost the catalytic performance of FTS catalysts, providing a conceptual advance to achieve higher carbon usage effectiveness by reducing  $\text{CO}_2$  emission.

## 2. Experimental

### 2.1. Materials synthesis

The mixture of  $\text{Co}(\text{acac})_2$  and  $\text{Mn}(\text{acac})_3$  (the mole ratio of  $\text{Co}$  to  $\text{Mn}$  is from 10/1–1/7) was dispersed in benzylamine and heated to 220 °C with a continuous stirring. The reaction mixture was cooled to room temperature after 2 h. The precipitate was then collected by centrifugation, followed by washing with ethanol and drying at 60 °C in a vacuum drying oven for 6 h. The as-synthesized sample was denoted as  $\text{Co}_x\text{Mn}_y$  (X/Y is from 10/1–1/7).

$\text{CoO}$  nanocrystals were synthesized by thermal decomposition of  $\text{Co}(\text{acac})_2$  (7.6 mmol) in benzylamine (560 mmol) at 200 °C for 2 h. The precipitate was then collected by centrifugation, followed by washing with ethanol and drying at 60 °C in a vacuum drying oven for 6 h. The obtained sample was denoted as  $\text{CoO}$ .

To synthesize  $\text{MnO}$  nanocrystals, a similar procedure was used. A mixture of  $\text{Mn}(\text{acac})_3$  (7.6 mmol) and benzylamine (560 mmol) were placed in the flask. The reaction was heated at 200 °C for 2 h. After cooling down to room temperature, the product was precipitated with the addition of ethanol and collected by centrifugation. Then the product was reduced in  $\text{H}_2$  at 400 °C for 3 h. The obtained sample was denoted as  $\text{MnO}$ .

Before performance testing, all the catalysts were modified with  $\text{Na}$  promoter by impregnation  $\text{Na}_2\text{CO}_3$  aqueous solution. 1.0 g  $\text{Co}_x\text{Mn}_y$  nanocrystals and a certain amount of  $\text{Na}_2\text{CO}_3$  powder were dispersed in 100 ml mixture solution of deionized water and ethanol (ratio of 1:1).

After ultrasonicated for 2 h, followed by evaporation in a rotary evaporator at 90 °C for 1 h (50–90 °C with heating rate of 5 °C/30 min) under vacuum. The obtained sample was dried at 120 °C for 12 h. The  $\text{Na}$  content was 0.4 wt%.

### 2.2. Characterization

X-ray diffraction (XRD) patterns were obtained by a Bruker D8 powder diffractometer using  $\text{Cu-K}\alpha$  radiation operated at 40 kV and 40 mA and a Vantec-1 detector.

The size and morphology of samples were determined using a FEI Tecnai G20 transmission electron microscope operated at 200 kV and a Hitachi SU8000 field emission scanning electron microscope at an accelerating voltage of 15 kV. The particle size distribution for samples was calculated by more than 200 nanoparticles.

Ex-situ X-ray Photoelectron Spectroscopy (XPS) measurements were conducted by a VG Multilab 2000 photoelectron spectrometer equipped with  $\text{Al-K}\alpha$  radiation under vacuum at  $2 \times 10^{-6}$  Pa. All binding energies were calibrated using the C 1 s peak (284.6 eV) of the surface adventitious carbon. The exposure to  $\text{H}_2$  or syngas was done in a chamber. The solid samples were reduced at 300 °C in a  $\text{H}_2$  atmosphere (0.1 MPa) for 5 h. The reduced samples were loaded into the test chamber inside a glove box, and then the XPS data of  $\text{Co}_1\text{Mn}_3\text{-R}$  was collected. For investigate the FTS reaction on the  $\text{Co}_1\text{Mn}_3$  catalysts, the chamber was vacuumed again to eliminate the excess hydrogen, and syngas ( $\text{H}_2/\text{CO} = 1$ , 0.1 MPa) was introduced at 250 °C for 2 h and 50 h. Then, the XPS spectra was recorded following the above-mentioned procedures.

The X-ray absorption spectra (XAS) including X-ray absorption near-edge structure (XANES) and extended X-ray absorption fine structure (EXAFS) of the samples were collected at the Singapore Synchrotron Light Source (SSLS) center, where a pair of channel-cut Si (111) crystals was used in the monochromator. The storage ring was working at the energy of 2.5 GeV with average electron current of below 200 mA.

Hydrogen temperature-programmed desorption ( $\text{H}_2\text{-TPD}$ ) experiment was conducted on Zeton Altamira AMI-300 unit.  $\text{Co}_x\text{Mn}_y$  Catalysts were pretreated in flowing argon at 373 K for 1 h, and reduced in flowing hydrogen at 573 K for 5 h while the temperature increased from 373 to 573 K at a ramping rate of 10 K min<sup>-1</sup>. The sample was then cooled to 373 K under hydrogen flow and purged with argon at 373 K for 1 h to remove physisorbed hydrogen species. The temperature was then increased slowly from 373 K to 773 K, and held under flowing argon to desorb the remaining chemisorbed hydrogen. A TCD detector was used to register the desorption signal until it returned to the baseline. The TPD spectrum was integrated and the amount of chemisorbed hydrogen was determined by comparing with the mean areas of calibrated

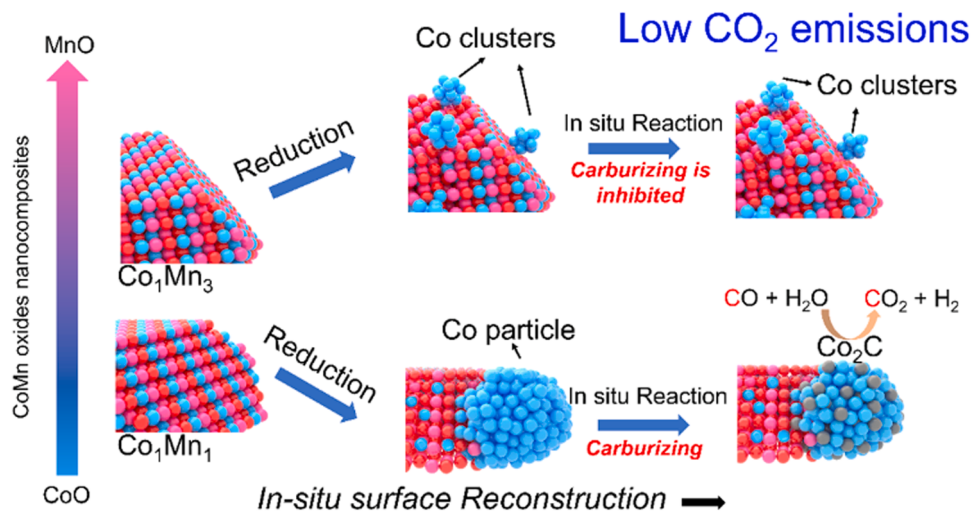


Fig. 1. Schematic models of the evolution of active phase in  $\text{Co}_1\text{Mn}_1$  (below) and  $\text{Co}_1\text{Mn}_3$  (above) catalyst.

hydrogen pulses.

The samples' compositions were analyzed by the inductively coupled plasma optic emission spectrometer (ICP-OES, Varian 720).

### 2.3. Catalytic reaction

Fischer-Tropsch synthesis was performed in a fixed-bed reactor with 1/4 in. inner-diameter stainless-steel tube. 0.1 g catalyst was diluted with 0.3 g quartz sand prior to testing. After reduction at 573 K by pure H<sub>2</sub> (8 SL g<sub>cat</sub><sup>-1</sup> h<sup>-1</sup>) for 5 h, the catalyst was cooled to 373 K in flowing H<sub>2</sub> before introduction of syngas (H<sub>2</sub> / CO / N<sub>2</sub> = 45 / 45 / 10, N<sub>2</sub> as internal standard). The gas hourly space velocity (GHSV) was maintained as 4 SL g<sub>cat</sub><sup>-1</sup> h<sup>-1</sup>, while the pressure was maintained at 0.1 MPa. The reaction temperature was then ramped slowly to 523 K. During reaction, the permanent gases (H<sub>2</sub>, CO, CO<sub>2</sub>) and light alkanes in the effluent of the reactor were monitored by an online gas chromatograph (Agilent 7890B, equipped with molecular sieves, Plot-Q and Al<sub>2</sub>O<sub>3</sub> capillary column). CO<sub>2</sub>, H<sub>2</sub>, CO, and N<sub>2</sub> were detected by thermal conductivity detector (TCD), while hydrocarbons were detected by Flame ionization detector (FID). The liquid products including oil and water were condensed in a cold trap (273 K). The oil products were analyzed using an Agilent 6890 N GC with a FID detector and a HP-5 column. The aqueous fraction was analyzed using an Agilent 4890 GC equipped with a FID detector and a HP-Innowax column. The product selectivity was calculated based on the carbon balance.

### 2.4. DFT calculations

Density functional theory (DFT) calculations were performed using generalized gradient approximation Perdew-Burke-Ernzerhof (PBE) functional [18] and projector-augmented wave (PAW) method [19] as implemented in Vienna ab initio simulation package (VASP) [20]. Second order Methfessel-Paxton electron smearing scheme (sigma = 0.2 eV) was used because of the metallic properties of Co and Co<sub>2</sub>C. Plane-wave kinetic energy cutoff of 400 eV was applied for the spin polarization calculations with the energy and force convergence criteria of 10–5 eV and 0.03 eV/Å, respectively. The bulk structures of hexagonal closely packed Co and orthorhombic Co<sub>2</sub>C were optimized with Monkhorst-Pack k-points of 14 × 10 × 10 and 16 × 16 × 10. The clusters in different sizes were truncated from the bulks. A thick vacuum of ca. 15 Å was added to each direction for screening the lateral interaction. The transition state (TS) structures were located by combining the climbing-image nudge elastic band (cNEB) and quasi-Newton minimizing techniques. Frequency calculations were used to confirm the TS structure with only one imaginary frequency.

## 3. Results and discussion

### 3.1. Co<sub>x</sub>Mn<sub>y</sub> oxides nanocomposites for FTO

A group of Co<sub>x</sub>Mn<sub>y</sub> oxide nanocomposites with different Co/Mn contents was synthesized via the one-pot thermal decomposition of a mixture of Co(acac)<sub>2</sub> and Mn(acac)<sub>3</sub> with different ratios in benzylamine

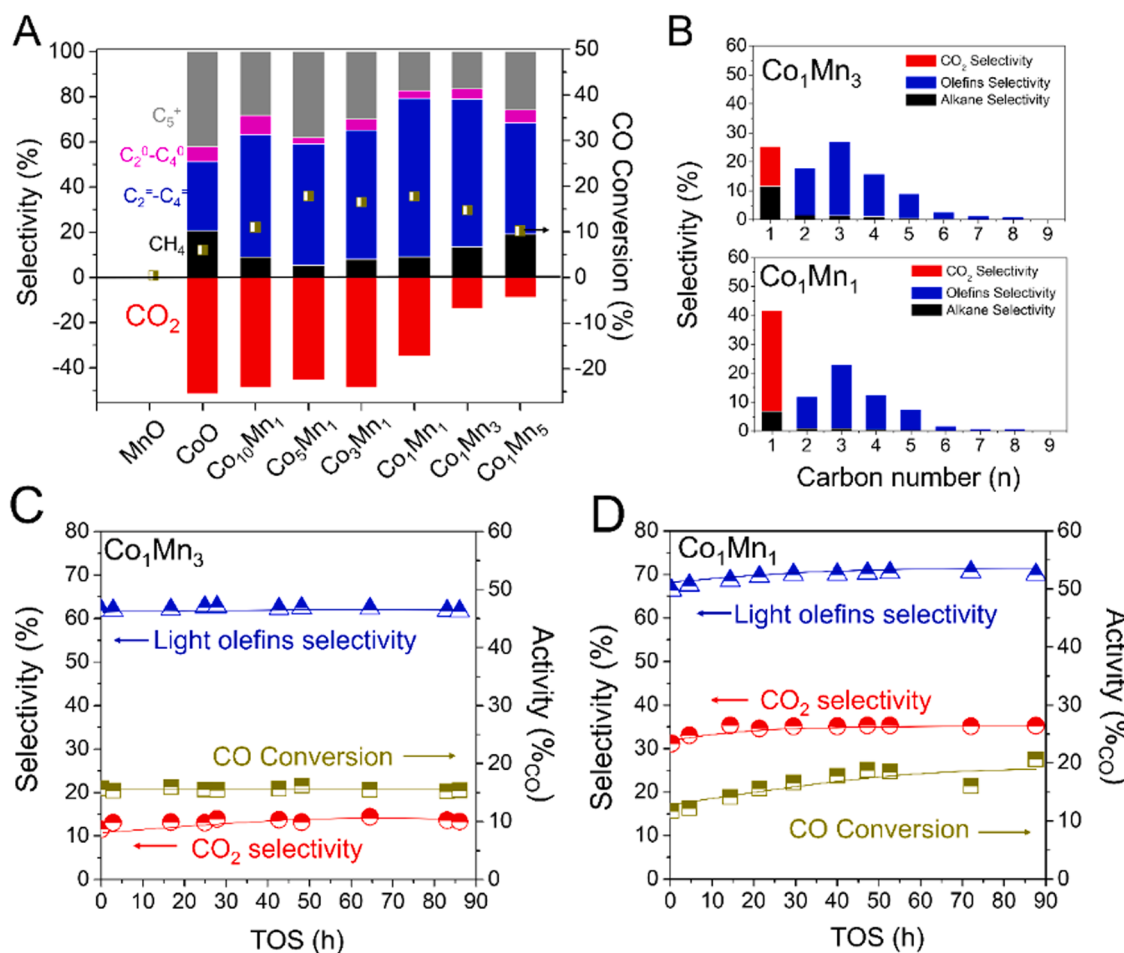


**Fig. 2.** Catalytic performance of different CoMn oxide nanocomposites catalysts. (A) Product distribution and CO conversion of different Co<sub>x</sub>Mn<sub>y</sub> catalysts. (B) Detailed product distribution (including CO<sub>2</sub>) over Co<sub>1</sub>Mn<sub>3</sub> and Co<sub>1</sub>Mn<sub>1</sub> catalysts. A stability test of (C) Co<sub>1</sub>Mn<sub>3</sub> catalyst and (D) Co<sub>1</sub>Mn<sub>1</sub> catalyst. Reaction condition: 250 °C, 0.1 MPa, H<sub>2</sub>/CO = 1.

at 220 °C, followed by the modification of Na promotor. The subscript x and y in  $\text{Co}_x\text{Mn}_y$  oxides represent the molar ratio of Co to Mn, which were determined by ICP-OES (Table S1). For blank comparison, pure CoO and MnO nanocrystal samples were also prepared. These samples were reduced at 300 °C with pure  $\text{H}_2$ , and then used for fixed-bed FTS with a  $\text{H}_2/\text{CO}$  ratio of 1:1 under the pressure of 0.1 MPa at 250 °C. Results in Fig. 2A and Table S2 show that CoO displays a low CO conversion of 6.0%, a light olefin selectivity of 30.6%, and a high  $\text{CO}_2$  selectivity of around 46.9%, whereas MnO shows no activity of FTS.

For all  $\text{Co}_x\text{Mn}_y$  oxide nanocomposites, the CO conversion is elevated to around ~15%. Specifically,  $\text{Co}_{10}\text{Mn}_1$  exhibits an improved light olefin selectivity of 54.1% and a  $\text{CO}_2$  selectivity of around 48.7%. As the increase of Mn fraction, both  $\text{Co}_5\text{Mn}_1$  and  $\text{Co}_3\text{Mn}_1$  demonstrate light olefin selectivity around 55.0%, but the  $\text{CO}_2$  selectivity is still as high as above ~45%. Interestingly, as the further increase of Mn fraction, the  $\text{Co}_1\text{Mn}_1$  catalyst shows a much improved light olefins selectivity of around 70.0% and an obviously reduced  $\text{CO}_2$  selectivity of 34.9%. Surprisingly, the  $\text{Co}_1\text{Mn}_3$  catalyst exhibits a light olefins selectivity of 65.4% and a remarkably low  $\text{CO}_2$  selectivity of only 13.7%. More importantly, the products are mainly  $\alpha$ -olefins, with olefin/paraffin molar ratio of 13.9 in the  $\text{C}_2^+$  hydrocarbons.

For the  $\text{Co}_1\text{Mn}_5$  catalyst with a higher Mn content, the  $\text{CO}_2$  selectivity is further reduced to 9.5%, but the methane selectivity increases to 19.0%, the CO conversion decreases to 10.2%, and the lower olefins selectivity decreases to 49.2%. The improved methane selectivity is possibly related to the size of the Co nanoparticles on the surface of the catalyst. [21] Among these catalysts, the  $\text{Co}_1\text{Mn}_3$  catalyst represents an unprecedented achievement of high selectivity towards light olefins and low selectivity towards  $\text{CO}_2$ .

The overall product distributions including  $\text{CO}_2$  are presented in Fig. 2B. Compared to  $\text{Co}_1\text{Mn}_1$ ,  $\text{Co}_1\text{Mn}_3$  demonstrates a much lower  $\text{CO}_2$  selectivity without affecting the selectivity toward lower olefins. The difference in the catalytic performances between  $\text{Co}_1\text{Mn}_3$  and  $\text{Co}_1\text{Mn}_1$  was further evaluated in the continuous FTO reaction over 90 h. As shown in Fig. 2C and D, the CO conversion and product distribution remain stable with time on steam for  $\text{Co}_1\text{Mn}_3$  samples. The CO conversion of  $\text{Co}_1\text{Mn}_1$  increases with time on steam. This change of CO conversion should be due to the phase change of  $\text{Co}_1\text{Mn}_1$  during the reduction and reaction. [15].

Moreover, temperature effect on catalytic performance of  $\text{Co}_3\text{Mn}_1$  and  $\text{Co}_1\text{Mn}_1$  catalyst are investigated, as shown in Table S3. The results show that CO conversion increased with the reaction temperature increasing, but the  $\text{CO}_2$  and  $\text{CH}_4$  selectivity increased significantly. Specifically, for  $\text{Co}_1\text{Mn}_3$ , the selectivity toward undesired  $\text{CO}_2$  is suppressed to be only 13.7% and the selectivity toward lower olefins

remains at ~60% by taking  $\text{CO}_2$  into account, during the 90 h continuous experiment. These differences in catalytic performance between  $\text{Co}_1\text{Mn}_3$  and  $\text{Co}_1\text{Mn}_1$  imply that there should be different active sites involved in the FTS reaction. Previous studies have suggested that for  $\text{Co}_1\text{Mn}_1$ , the generated  $\text{Co}_2\text{C}$  phase should act as the active site for FTS reaction [15,22]. Intriguingly, the active site in  $\text{Co}_1\text{Mn}_3$  needs further elucidation.

### 3.2. Catalysts structure and structure evolution

We started our investigation from examining the crystalline structures of these samples by XRD. Fig. 3A shows that for CoO, the diffraction peaks at 36.5°, 42.4°, and 61.5° are attributed to the (111), (200), and (220) planes of the fcc CoO (Fm3m,  $a = 4.26 \text{ \AA}$ , JCPDS 48-1719). For MnO, the diffraction peaks at 34.9°, 40.5°, and 58.7° are attributed to the (111), (200), and (220) planes the fcc MnO (Fm3m,  $a = 4.44 \text{ \AA}$ , JCPDS 78-0424). With respect to the  $\text{Co}_x\text{Mn}_y$  oxide nanocomposites, the diffraction peaks shift gradually between the peaks of CoO and MnO as the molar ratio of Co/Mn varies, while maintaining the fcc phase structure. These results suggest a uniform crystalline structure of the  $\text{Co}_x\text{Mn}_y$  oxide nanocomposites regardless of the metal fraction from  $\text{Co}_{10}\text{Mn}_1$  to  $\text{Co}_1\text{Mn}_3$ . The further increase of Mn content results in the formation of  $\text{Mn}_3\text{O}_4$  (Fig. S1 for the XRD patterns of  $\text{Co}_1\text{Mn}_5$  sample).

TEM images of  $\text{Co}_x\text{Mn}_y$  oxide nanocomposites with different Co/Mn contents show nanocrystals with size of 10–20 nm and excellent dispersion and uniformity (Fig. S2). Moreover, a high-angle annular dark-field (HAADF) image of the representative  $\text{Co}_1\text{Mn}_1$  sample (Fig. S3a) shows the uniform distribution of octahedron nanocrystals. The corresponding EDX mappings of  $\text{Co}_1\text{Mn}_1$  (Fig. S3b-d) confirm the uniform distribution of both Co and Mn elements in the nanocrystals. These  $\text{Co}_x\text{Mn}_y$  oxide nanocomposites show similar morphologies but dramatically different catalytic performances, especially different  $\text{CO}_2$  selectivity, presumably indicating distinct structural evolution during reduction and FTS reaction.

The reduction behavior of these  $\text{Co}_x\text{Mn}_y$  oxide nanocomposites were examined by  $\text{H}_2$ -TPR. Fig. 3B shows that all samples except MnO exhibit two distinct peaks, i.e., a peak from 260 to 420 °C ascribing to the reduction of the surface  $\text{Co}_3\text{O}_4$  species, and a peak from 420 to 650 °C attributing to the reduction of  $\text{Co}^{2+}$  to  $\text{Co}^0$  [23]. The obvious shift of both peaks to higher temperature suggests that the reduction becomes more difficult as the increase of Mn content. For pure MnO, reduction signal is barely observed in Fig. 3B.

After reduction, these samples, with new names containing a suffix of -R, were re-characterized by XRD. Fig. S4 shows that from the sample of  $\text{Co}_{10}\text{Mn}_1$ -R to  $\text{Co}_1\text{Mn}_1$ -R, both diffraction peaks of  $\text{Co}_x\text{Mn}_{1-x}\text{O}$  and metal

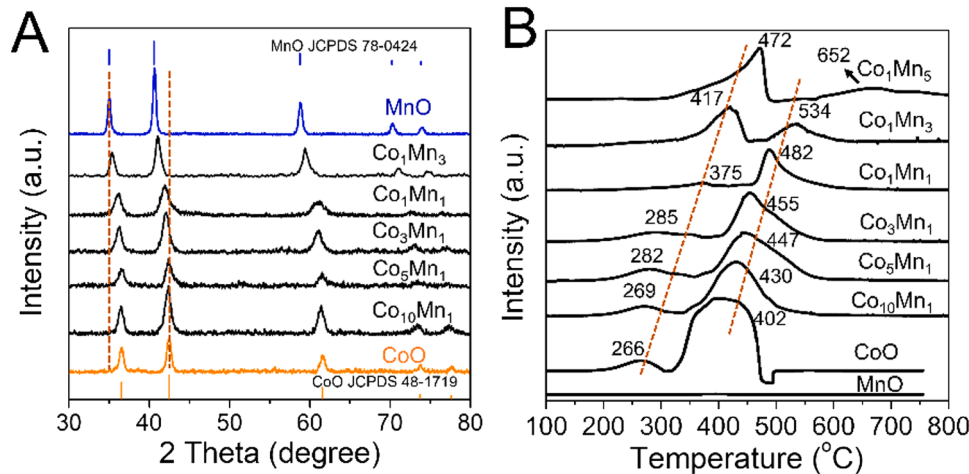


Fig. 3. Structure of CoMn oxides nanocomposites. (A) XRD pattern of different  $\text{Co}_x\text{Mn}_y$  catalysts. (B)  $\text{H}_2$ -TPR profiles of different  $\text{Co}_x\text{Mn}_y$  oxides nanocomposites, pure CoO and MnO sample.

Co are observed, but with decreasing Co signals. This result implies that crystalline Co nanoparticles are generated after the reduction process and formed from the surface of the CoMn oxides, generating  $\text{Co}_x\text{Mn}_{1-x}\text{O}$  nanocomposites. Moreover, the diffraction peaks of  $\text{Co}_x\text{Mn}_{1-x}\text{O}$  gradually shift to smaller angle during the reduction process. These results from  $\text{H}_2\text{-TPR}$  and XRD are consistent that as the decrease of Co content in the  $\text{Co}_x\text{Mn}_y$  oxide nanocomposites, the reduction of CoMn oxide to form Co metal with long-range order becomes more difficult. In contrast, for the  $\text{Co}_1\text{Mn}_3\text{-R}$  catalyst with a high lower olefins selectivity and a lower  $\text{CO}_2$  selectivity, no metal Co signal could be observed, suggesting that Co nanoparticles are not generated after reduction. The active surface sites of the  $\text{Co}_1\text{Mn}_3\text{-R}$  catalyst need further characterizations, which will be presented later.

### 3.3. Structure analysis of spent catalysts

After the FTS reaction, these catalysts were given new names containing a suffix of -S and were examined by XRD for the third time. Fig. S5 shows that from  $\text{Co}_{10}\text{Mn}_1\text{-S}$  to  $\text{Co}_1\text{Mn}_1\text{-S}$ , both diffraction peaks of  $\text{Co}_x\text{Mn}_{1-x}\text{O}$  and  $\text{Co}_2\text{C}$  are observed. The generation of  $\text{Co}_2\text{C}$  is because

of the carbonization of metal Co during FTO reaction, which has been demonstrated in previous studies [23,24]. Interestingly, in the  $\text{Co}_1\text{Mn}_3\text{-S}$  sample, the  $\text{Co}_2\text{C}$  phase is not present. These results are consistent with the fact that the signal of metal Co is not observed in Fig. S4 and further verify our hypothesis that the structural evolution during reduction and FTS reaction of  $\text{Co}_1\text{Mn}_3$  is different from that of other  $\text{Co}_x\text{Mn}_y$  samples.

In the following sections, we will explore the difference of the two samples, i.e.,  $\text{Co}_1\text{Mn}_3$  and  $\text{Co}_1\text{Mn}_1$  as the representative of other  $\text{Co}_x\text{Mn}_y$  samples, to elucidate the structural origin of the superior catalytic performance of  $\text{Co}_1\text{Mn}_3$ . The structural difference between the  $\text{Co}_1\text{Mn}_3$  and  $\text{Co}_1\text{Mn}_1$  was confirmed by HRTEM characterization on the spent samples after FTO reaction. For  $\text{Co}_1\text{Mn}_3\text{-S}$ , Figs. S6a to 6c show the uniform distribution of Co elements in the  $\text{Co}_x\text{Mn}_{1-x}\text{O}$  nanocomposite, while  $\text{Co}_2\text{C}$  is not observed. For  $\text{Co}_1\text{Mn}_1\text{-S}$ , Figs. S6d to 6f show an apparent migration of the Co species to the surface of the  $\text{Co}_x\text{Mn}_{1-x}\text{O}$  nanocomposite to form  $\text{Co}_2\text{C}$  moiety. The  $\text{Co}_2\text{C}$  nanoprisms contribute to the high  $\text{C}_{2-4}$  selectivity and  $\text{CO}_2$  selectivity, which is consistent with previous study [15].

In order to reveal the fine atomic structure, X-ray adsorption near-edge structure (XANES) and extended X-ray adsorption fine structure

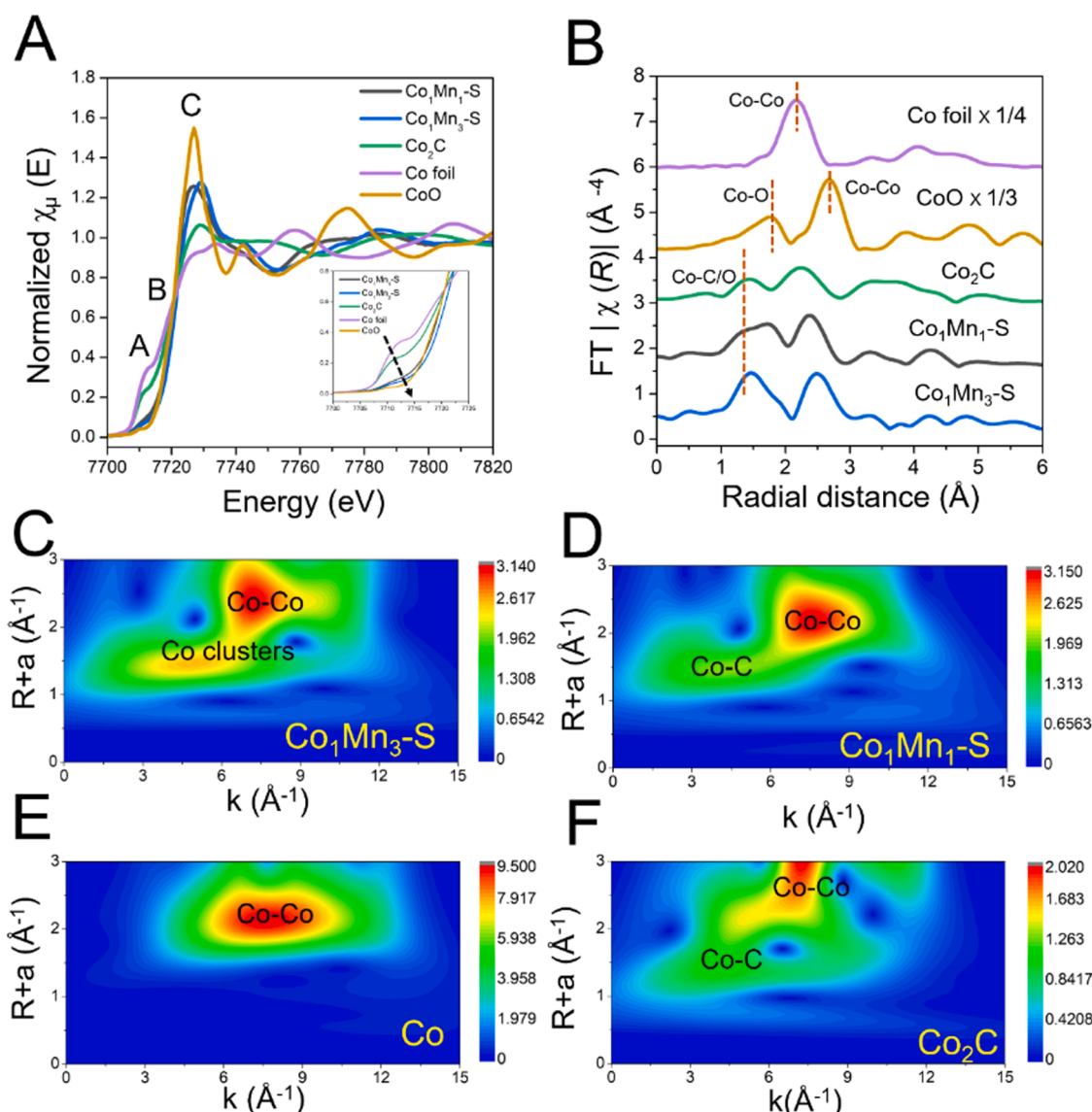


**Fig. 4.** XAS characterization of spent CoMn oxides nanocomposites. (A) Co K-edge XANES spectra of different  $\text{Co}_x\text{Mn}_y\text{-S}$  samples and reference of Co foil,  $\text{Co}_2\text{C}$  and  $\text{CoO}$ . (B) Fourier transform spectra for the used catalyst and reference of Co foil and  $\text{CoO}$  sample. (C)-(F) Wavelet transforms for  $\text{Co}_1\text{Mn}_3\text{-S}$ ,  $\text{Co}_1\text{Mn}_1\text{-S}$ , Co foil and  $\text{Co}_2\text{C}$ , respectively.

(EXAFS) characterizations were performed on  $\text{Co}_1\text{Mn}_3\text{-S}$  and  $\text{Co}_1\text{Mn}_1\text{-S}$  samples after FTS reaction. The Co K-edge XANES spectra are shown in Fig. 4A, with Co foil and standard  $\text{CoO}$  and  $\text{Co}_2\text{C}$  as references. The spectra contain a weak pre-edge peak A, a shoulder peak B on the rising edge, and a sharp white-line peak C. The position of peak A is related to the valence state of the element, where the peak at higher energy implies a higher oxidation state [25]. The valences of Co in both  $\text{Co}_1\text{Mn}_3\text{-S}$  and  $\text{Co}_1\text{Mn}_1\text{-S}$  are slightly lower than +2, suggesting the reduction of Co element after the FTO reaction. Moreover, the peak A of  $\text{Co}_1\text{Mn}_1\text{-S}$  resembles that of  $\text{Co}_2\text{C}$ , confirming that the  $\text{Co}_2\text{C}$  is the active site [26].

The FT-EXAFS spectra of these samples are shown in Fig. 4B. The  $\text{Co}_1\text{Mn}_1\text{-S}$  sample shows signals that are very close to  $\text{Co}_2\text{C}$ . Interestingly, the  $\text{Co}_1\text{Mn}_3\text{-S}$  sample exhibits a peak at the R distance of 1.5 Å, which is between the signal of Co-C/O of  $\text{Co}_2\text{C}$  at 1.4 Å and the signal of Co-O of  $\text{CoO}$  at 1.8 Å. This peak is speculated to be from a new Co structure that is different from  $\text{Co}_2\text{C}$  and  $\text{CoO}$ . Such information is also validated by the data fitting (Fig. S7 and S8) and the structural parameters extracted from the data fitting in Table S4.

Moreover, the wavelet transforms (WT) contour plots at the first and second shells of the  $\text{Co}_1\text{Mn}_3\text{-S}$  and  $\text{Co}_1\text{Mn}_1\text{-S}$  samples are shown in Fig. 4C and D. It is obvious that both samples exhibit good metallic characters, showing a Co-Co shell at around 6.5 Å<sup>-1</sup> which is close to

that of Co foil (Fig. 4E). Compared with the Co foil, the  $\text{Co}_1\text{Mn}_3\text{-S}$  sample could be well fitted to Co clusters, which will be verified later. For  $\text{Co}_1\text{Mn}_1\text{-S}$ , it is observed that a  $\text{Co}_2\text{C}$  phase with a Co-C/O shell at 4.2 Å<sup>-1</sup> (Fig. 4F) appears.

### 3.4. Surface reconstruction of $\text{Co}_1\text{Mn}_3$ and $\text{Co}_1\text{Mn}_1$ catalyst

The  $\text{Co}_1\text{Mn}_3$  sample at different stages, i.e., the fresh  $\text{Co}_1\text{Mn}_3$ , the reduced  $\text{Co}_1\text{Mn}_3\text{-R}$ , and two samples at different FTS reaction time  $\text{Co}_1\text{Mn}_3\text{-S-2 h}$  (after reaction of 2 h) and  $\text{Co}_1\text{Mn}_3\text{-S-50 h}$  (after reaction of 50 h), were further examined by ex-situ XPS characterization in order to probe the active site involved. Fig. 5A shows the evolution of the Co 2p spectra at different stages. For the fresh  $\text{Co}_1\text{Mn}_3$ , the peaks at 781.1 and 780.2 eV could be attributed to the characteristic signals of  $\text{Co}^{2+}$  and  $\text{Co}^{3+}$ , respectively [27], whereas the peak at 782.4 eV could be assigned to the  $\text{Co}^{2+}$  in hydroxide. After the reduction treatment at 300 °C for 5 h, the  $\text{Co}_1\text{Mn}_3\text{-R}$  exhibits a new peak at 778.2 eV, ascribing to the generation of  $\text{Co}^0$  clusters on the surface of the catalyst [28]. This  $\text{Co}^0$  signal preserves in both of the two  $\text{Co}_1\text{Mn}_3\text{-S-2 h}$  and  $\text{Co}_1\text{Mn}_3\text{-S-50 h}$  samples after FTS reaction. This result complies with the conclusion from the EXAFS experiments that a new  $\text{Co}^0$  cluster phase appears in  $\text{Co}_1\text{Mn}_3$ , affording key role in the FTS reaction. These  $\text{Co}^0$  clusters are

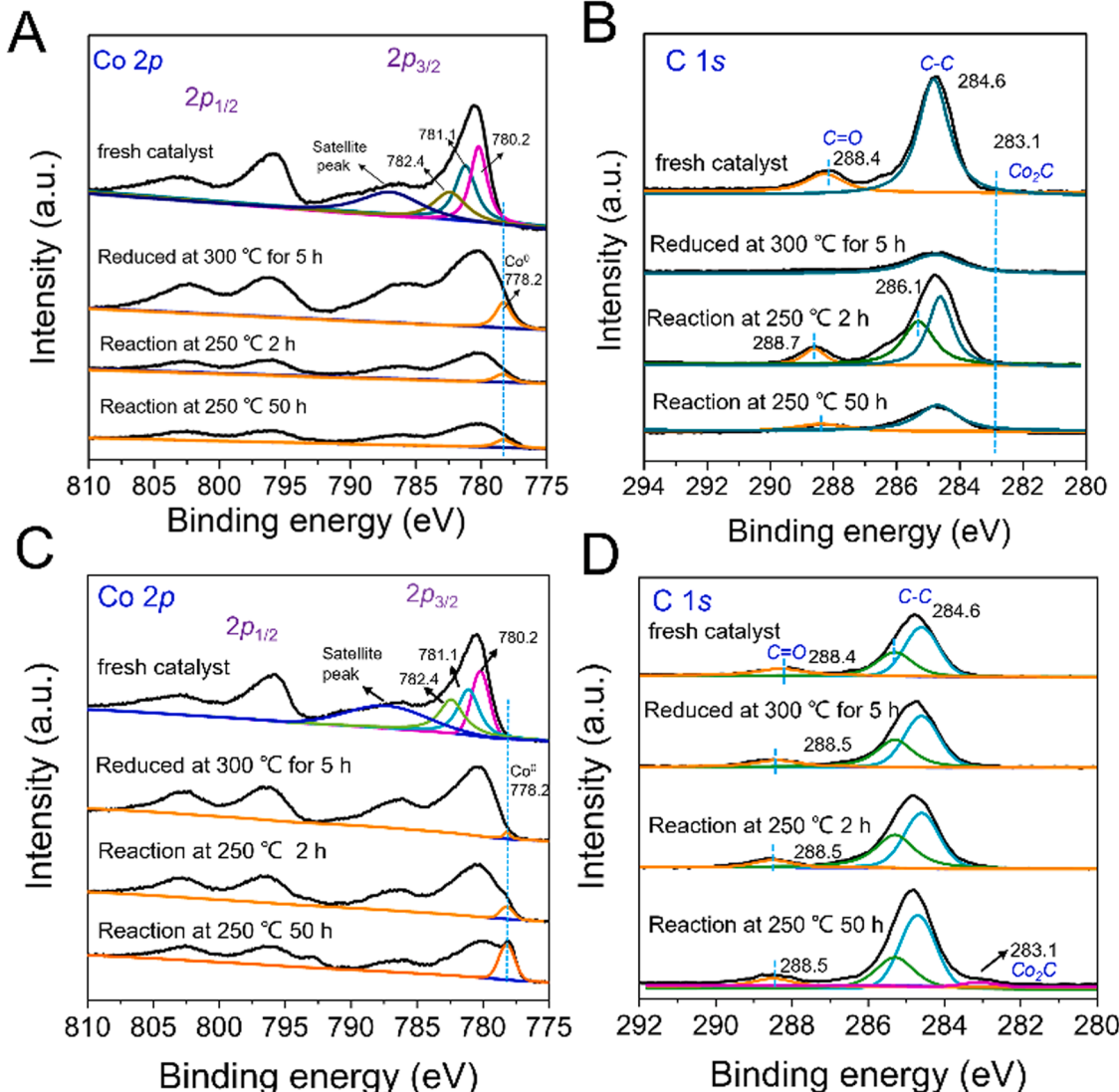


**Fig. 5.** Ex-situ XPS spectra for CoMn catalysts. (A) Co 2p and (B) C 1s regions of  $\text{Co}_1\text{Mn}_3$  catalyst under different conditions. (C) Co 2p and (D) C 1s regions of  $\text{Co}_1\text{Mn}_1$  catalyst under different conditions. Reduction condition:  $\text{H}_2$ , 300 °C, 5 h; Reaction condition: 250 °C, 0.1 MPa,  $\text{H}_2$  /  $\text{CO}$  = 1.

generated from the  $\text{Co}_1\text{Mn}_3$  oxides nanocomposites and stabilized on the surface of the  $\text{Co}_x\text{Mn}_{1-x}\text{O}$  oxides. The size of these  $\text{Co}^0$  clusters is too small to be observed by XRD, explaining the absence of the crystalline Co diffraction patterns in  $\text{Co}_1\text{Mn}_3\text{-R}$  and  $\text{Co}_1\text{Mn}_3\text{-S}$ .

Previous TPR and XRD characterizations (Fig. 3) have revealed that the interaction between Co and Mn in the CoMn oxides nanocomposites is enhanced with the increase of Mn content. Consequently, we suspect that the formation of crystalline Co nanoparticles in the  $\text{Co}_1\text{Mn}_3\text{-R}$  sample is not favored due to the higher Mn content. Notably, there is no signal of  $\text{Co}_2\text{C}$  in  $\text{Co}_1\text{Mn}_3\text{-S}$  for the whole process even after 50 h FTS reaction, suggesting the dominant role of  $\text{Co}^0$  cluster as the active phase in  $\text{Co}_1\text{Mn}_3$ . de Jong et al. concluded that while  $\text{Co}/\text{Mn} \approx 0.3$ , the metallic Co could be well dispersed and stabilized by the  $\text{Mn}_x$  support during FTS reaction [29].

Fig. 5B shows the evolution of C 1 s spectra of the  $\text{Co}_1\text{Mn}_3$  sample at different stages. For the fresh  $\text{Co}_1\text{Mn}_3$ , the peaks at around 288.4 and 284.6 eV are attributed to the C=O and C-C, respectively, of carbonate formed in the preparation process. After the reduction treatment, the above two peaks disappear in  $\text{Co}_1\text{Mn}_3\text{-R}$ . Interestingly, during the FTS reaction at 2 h, new peaks at 286.1 and 288.7 eV appear in  $\text{Co}_1\text{Mn}_3\text{-S}$ -2 h, ascribing to the C-O of adsorption CO molecular and  $^*\text{HCOO}$  intermediate [30], respectively. This result suggests the CO adsorption and further transformation of CO on the surface of the  $\text{Co}_1\text{Mn}_3$  catalyst. As the reaction proceeds to 50 h, the  $\text{Co}_1\text{Mn}_3\text{-S}$ -50 h exhibits a small peak at 288.4 eV, corresponding to the carbonate products generated in FTS reaction. Moreover, no signal attributed to  $\text{Co}_2\text{C}$  was observed in Fig. 5A and B, confirming that the active phase of  $\text{Co}_1\text{Mn}_3$  catalyst was  $\text{Co}^0$  clusters rather than  $\text{Co}_2\text{C}$ .

For comparison, ex-situ XPS spectra for  $\text{Co}_1\text{Mn}_1$  catalysts was shown in Fig. 5C and D. A peak of Co 2p at 778.0 eV appears after being reduced, indicating the formation of  $\text{Co}^0$  on the surface of the catalyst. As the reaction time of 2 h, the  $\text{Co}^0$  peak intensifies obviously. At 50 h, many  $\text{Co}_2\text{C}$  nanoparticles are generated, showing a strong  $\text{Co}^0$  peak [31, 32]. The formation of  $\text{Co}_2\text{C}$  could also be verified by the C1s signal of the XPS results, where a new peak at 283.1 eV appears in  $\text{Co}_1\text{Mn}_1$ -50 h that is ascribed to the carbon in  $\text{Co}_2\text{C}$ . These results show that two possible active phases exist in the  $\text{Co}_1\text{Mn}_1$  catalyst, i.e.,  $\text{Co}^0$  and  $\text{Co}_2\text{C}$ , which is consistent with the XRD, TEM, and EXAFS results.

### 3.5. DFT calculation on $\text{Co}^0$ clusters

Density functional theory (DFT) calculations were further carried out to examine why the formation of  $\text{Co}^0$  cluster is preferred to  $\text{Co}_2\text{C}$  in  $\text{Co}_1\text{Mn}_3$  by calculating the carbon potential ( $\mu$ ), which is a descriptor for interpreting the thermodynamic feasibility of carburization of transition metals, of  $\text{Co}^0$  cluster with different size and  $\text{Co}_2\text{C}$ . Fig. 6A shows the

critical  $\mu$  values, i.e.,  $\mu_{cri} = E_{\text{Co}2\text{C}} - 2E_{\text{Co}}$ , to represent the minimum value to maintain the stable truncated nanoclusters ( $\text{Co}_{20}\text{C}_{10}$ ,  $\text{Co}_{48}\text{C}_{24}$ , and  $\text{Co}_{144}\text{C}_{72}$ ) and bulk  $\text{Co}_2\text{C}$ . It is observed that all the  $\text{Co}_2\text{C}$  clusters exhibit larger  $\mu_{cri}$  values ( $> -7.33$  eV) than that ( $\mu_{FTS} = -8.14$  eV) in typical FTS reaction, indicating that  $\text{Co}_2\text{C}$  clusters are not stable under FTS conditions [33]. It is thus inferred that the carburization of small cobalt clusters is not favored during the FTS reactions, which is consistent with our experimental observations.

Moreover, DFT calculations were performed to understand the improved production of olefins. The reaction pathways of two consecutive hydrogenation of C=C bond are illustrated in Fig. 6B. The first step of C=C hydrogenation occurs easily with rate-limiting energy barrier of ca. 0.53 eV for  $\text{Co}_{48}$  cluster. However, a much higher rate-limiting barrier of ca. 1.07 eV is obtained for second step hydrogenation in the presence of sodium, resulting in significant suppression of the olefin hydrogenation.

### 3.6. Reaction mechanism over $\text{Co}^0$ clusters/ $\text{Co}_x\text{Mn}_{1-x}\text{O}$ catalyst

In traditional FTS reactions, previous studies have suggested that the active metallic Co nanoparticles could facilitate the C-C coupling reaction, resulting in high selectivity toward long-chain alkanes [34]. Interestingly, our  $\text{Co}_1\text{Mn}_3$  catalyst shows a lower  $\text{C}_5^+$  selectivity of 16.5%, with a chain growth factor ( $\alpha$ ) of only 0.43. The ASF plot of the product distribution over  $\text{Co}_1\text{Mn}_3$  catalyst is presented in Fig. 7A, showing that the distribution of the  $\text{CH}_x$  species still obeys the probabilistic polymerization mechanism, but the probability of carbon chain growth drops significantly. The chain growth of the  $\text{CH}_x$  monomers species is considered to be at stepped B5 sites, which are generally composed of four atoms in the same plane and one atom in the other plane [35]. And high chain growth requires a catalyst with active phase of a certain size [36].

To confirm the size of the  $\text{Co}^0$  clusters, we characterized the  $\text{Co}_1\text{Mn}_3\text{-S}$  sample using atomic-resolution high-resolution high-angle annular dark-field scanning transmission electron microscopy (HAADF-STEM). Fig. 7B shows that the  $\text{Co}^0$  clusters are 0.8–1 nm in size. These subnanometer sized  $\text{Co}^0$  clusters should pose a huge steric hindrance for the C-C coupling process, resulting in a low chain growth probability as shown in Fig. 7A.

There is another important issue regarding the regulation of methane selectivity. It has been demonstrated that Co nanoparticles with smaller size are more likely to generate methane [21]. de Jong et al. found that when the size of Co nanoparticles is smaller than 3.0 nm, the methane selectivity could reach as high as 53.0%, due to the higher H coverage and lower CO coverage on the surface of small Co nanoparticles [37]. However, for the  $\text{Co}^0$  clusters with sub-nanometer size in this study, the

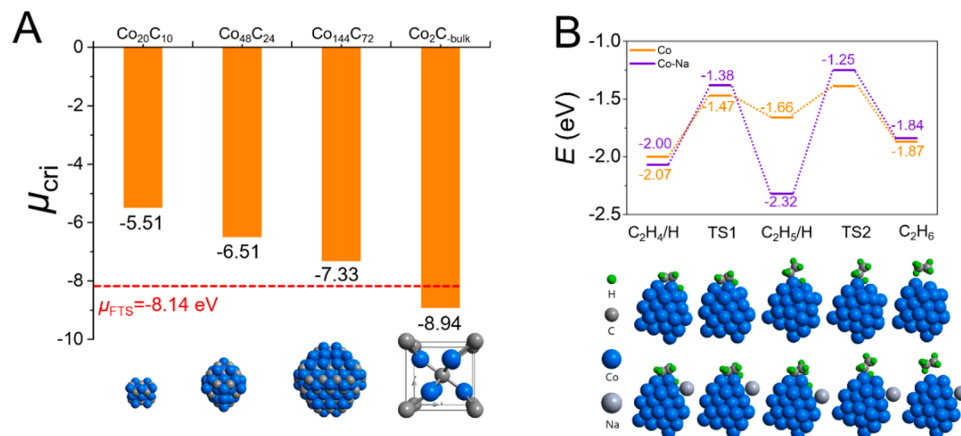
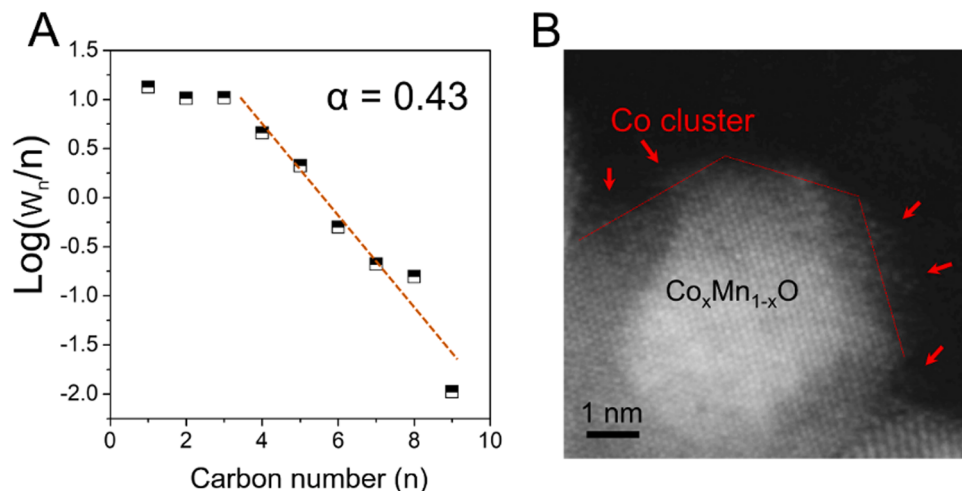


Fig. 6. DFT calculations on the catalytic behavior of Co clusters. (A) The critical carbon potential of  $\text{Co}_2\text{C}$  clusters and bulk predicted by DFT calculations. (B) The reaction pathways of two consecutive hydrogenation of C=C bond on Co and Co-Na.



**Fig. 7.** Catalytic performance and structure characterization for  $\text{Co}_1\text{Mn}_3$  catalyst. (A) Anderson-Schulz-Flory (ASF) plot of hydrocarbon products over  $\text{Co}_1\text{Mn}_3$  catalyst. (B) Atomic-resolution high-resolution high-angle annular dark-field scanning transmission electron microscopy (HAADF-STEM) of spent  $\text{Co}_1\text{Mn}_3$ -S catalyst.

methane selectivity is below to 13.5% even at a high reaction temperature of 250 °C and the lower olefins selectivity reaches 65.4% with the overall O/P ratio as high as 13.9. These results reveal that the H coverage on the  $\text{Co}^0$  clusters has been greatly improved and the hydrogenation process has been inhibited. This is closely related to the unique electronic environment of the  $\text{Co}_1\text{Mn}_3$  catalyst surface. Due to the unique surrounding Mn environments, these active  $\text{Co}^0$  clusters could facilitate the adsorption of CO and inhibit the hydrogenation reaction, favoring the olefins production [29].

Results from the ex-situ Mn 2p XPS spectra (Fig. S9) further reveal the electron-rich status of the catalyst surface. In the fresh  $\text{Co}_1\text{Mn}_3$  sample, the main valence states of Mn are +3/+4 with a peak centered at 642.1 eV, due to the partial oxidation of the catalyst surface during sample preparation [38]. After the reduction treatment, the Mn 2p<sub>3/2</sub> peak in  $\text{Co}_1\text{Mn}_3$ -R shifts to 640.3 eV, indicating that the valance states of Mn is +2 [39]. During the FTO reaction,  $\text{Co}_1\text{Mn}_3$ -S-2 h sample shows a shift of the peak to higher binding energy of 640.6 eV, which continues to increase to 640.8 eV in  $\text{Co}_1\text{Mn}_3$ -S-50 h. These results suggest a continuous loss of electron of the Mn atoms during the FTS reaction. These donated electrons from Mn could effectively reduce the  $\text{H}_2$  coverage on the catalyst surface and suppress the hydrogenation reaction of olefins [40].

Notably, the role of Na promoter is also key to the high selectivity towards lower olefins and relatively low selectivity towards methane of the  $\text{Co}_1\text{Mn}_3$  catalyst. We further verified this point by carrying out  $\text{H}_2$ -TPD experiments. Fig. S10 shows that the Na modification greatly decreases the amount of  $\text{H}_2$  desorption by the  $\text{Co}_1\text{Mn}_3$  catalyst from 598.6 mmol/g<sub>cat</sub> (before Na modification) to 507 mmol/g<sub>cat</sub> (after Na modification). This result indicates that the Na modification could greatly inhibit the adsorption of  $\text{H}_2$  and thus promote the adsorption of CO, resulting in a higher O/P ratio in the overall product. Moreover, the Na promoter, which acts as an electronic donor to cobalt clusters, would accelerates lower olefins desorption and also suppresses the secondary hydrogenation of olefins [23]. Therefore, the smaller particle size and low H coverage of  $\text{Co}^0$  clusters result in a low  $\alpha$  value and a higher O/P ratio, rendering the  $\text{Co}_1\text{Mn}_3$  catalyst to achieve a selectivity of 65.4% for lower olefins.

More importantly, the  $\text{Co}^0$  cluster has a low activity to catalyze water-gas shift reaction, resulting in minimum formation of  $\text{CO}_2$ . The conversion of syngas using the  $\text{Co}^0$  clusters/ $\text{Co}_x\text{Mn}_{1-x}\text{O}$  catalyst toward highly selectively formation of lower olefins while suppressing the formation of  $\text{CO}_2$  are illustrated in Fig. 8. Our experimental and theoretical results conclude that the formation of stable  $\text{Co}^0$  clusters on the surface of  $\text{Co}_x\text{Mn}_{1-x}\text{O}$  nanocomposite is key to the superior selectivity toward

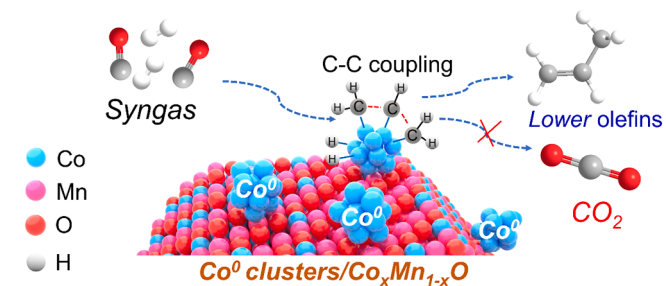


**Fig. 8.** Catalytic reaction mechanism for syngas conversion. Illustration of the reaction of syngas conversion to lower olefins over  $\text{Co}^0$  clusters/ $\text{Co}_x\text{Mn}_{1-x}\text{O}$  catalyst.

lower olefins, while exhibiting remarkably low  $\text{CO}_2$  selectivity in FTS reactions.

#### 4. Conclusions

It is of paramount importance to improve the selectivity toward light olefins while reducing the formation of  $\text{CO}_2$  and methane as much as possible in FTS reactions, achieving efficient carbon utilization. Current efforts have been challenged by the high  $\text{CO}_2$  formation, which detriments the overall carbon usage. In this study, we report a CoMn oxide nanocomposite, namely  $\text{Co}_1\text{Mn}_3$ , with a remarkably high  $\text{C}_2\text{-C}_4$  selectivity of 65.4% and an extremely low  $\text{CO}_2$  selectivity of only 13.7%. Taking the generated  $\text{CO}_2$  into account, the overall carbon selectivity toward lower olefins ~60%. This sample also exhibits excellent stability during a continuous FTS reaction for 90 h. Results from a comprehensive set of experimental and theoretical experiments reveal that metallic  $\text{Co}^0$  clusters are generated on the surface of the catalyst due to the reduction treatment. These  $\text{Co}^0$  clusters are thermodynamically more stable than  $\text{Co}_2\text{C}$ , which has been suggested to be the active phase in FTO in previous studies. The  $\text{Co}^0$  cluster rather than  $\text{Co}_2\text{C}$  as active phase facilitates the formation of lower olefins while inhibiting the formation of  $\text{CO}_2$ , rendering the unprecedently high carbon usage toward lower olefins. This work provides a new mechanistic understanding on the manipulation of the active phase of Co-based catalysts for improving the selectivity toward desirable products at high carbon usage.

#### Funding

This work was supported by the National Natural Science Foundation

of China (No. 22072184, 22102220, and 21972170), the Young Top-notch Talent Cultivation Program of Hubei Province.

### CRediT authorship contribution statement

**Shuai Lyu:** Methodology, Investigation, Writing - original draft. **Qingsen Wu:** Investigation, Methodology. **Zhe Li:** Investigation, Visualization. **Yuhua Zhang:** Investigation, Methodology. **Jinlin Li:** Conceptualization, Funding acquisition, Validation. **Li Wang:** Supervision, Conceptualization, Funding acquisition, Methodology, Writing - review & editing.

### Declaration of Competing Interest

The authors declare that they have no known competing financial interests or personal relationships that could have appeared to influence the work reported in this paper.

### Data availability

Data will be made available on request.

### Appendix A. Supporting information

Supplementary data associated with this article can be found in the online version at [doi:10.1016/j.apcatb.2022.122347](https://doi.org/10.1016/j.apcatb.2022.122347).

### References

- [1] A. Boulamanti, J.A. Moya, Production costs of the chemical industry in the EU and other countries: ammonia, methanol and light olefins, *Renew. Sustain. Energy Rev.* 68 (2017) 1205–1212, <https://doi.org/10.1016/j.rser.2016.02.021>.
- [2] S. Xiang, Z. Zhang, C. Zhao, K. Hong, X. Zhao, D. Ding, M. Xie, C. Wu, M.C. Das, R. Gill, K.L. Thomas, B. Chen, Rationally tuned micropores within enantiopure metal-organic frameworks for highly selective separation of acetylene and ethylene, *Nat. Commun.* 2 (2011) 204–210, <https://doi.org/10.1038/ncomms1206>.
- [3] H.M. Torres Galvis, K.P. de Jong, Catalysts for production of lower olefins from synthesis gas: a review, *ACS Catal.* 3 (2013) 2130–2149, <https://doi.org/10.1021/cs4003436>.
- [4] J. Li, Y.L. He, L. Tan, P.P. Zhang, X.B. Peng, A. Oruganti, G.H. Yang, H. Abe, Y. Wang, N. Tsubaki, Integrated tuneable synthesis of liquid fuels via Fischer-Tropsch technology, *Nat. Catal.* 1 (2018) 787–793, <https://doi.org/10.1038/s41929-018-0144-z>.
- [5] W. Zhou, K. Cheng, J. Kang, C. Zhou, V. Subramanian, Q. Zhang, Y. Wang, New horizon in C1 chemistry: breaking the selectivity limitation in transformation of syngas and hydrogenation of CO<sub>2</sub> into hydrocarbon chemicals and fuels, *Chem. Soc. Rev.* 48 (2019) 3193–3228, <https://doi.org/10.1039/C8CS00502H>.
- [6] A.Y. Khodakov, W. Chu, P. Fongarland, Advances in the development of novel cobalt Fischer-Tropsch catalysts for synthesis of long-chain hydrocarbons and clean fuels, *Chem. Rev.* 107 (2007) 1692–1744, <https://doi.org/10.1021/cr050972v>.
- [7] P. Zhai, C. Xu, R. Gao, X. Liu, M. Li, W. Li, X. Fu, C. Jia, J. Xie, M. Zhao, X. Wang, Y. Li, Q. Zhang, X. Wen, D. Ma, Highly tunable selectivity for syngas-derived alkenes over zinc and sodium-modulated Fe<sub>5</sub>C<sub>2</sub> catalyst, *Angew. Chem. Int. Ed.* 128 (2016) 10056–10061, <https://doi.org/10.1002/ange.201603556>.
- [8] G. Henrici-Olivé, S. Olive, The Fischer-Tropsch synthesis: molecular weight distribution of primary products and reaction mechanism, *Angew. Chem. Int. Ed. Engl.* 15 (1976) 136–141, <https://doi.org/10.1002/anie.197601361>.
- [9] K. Cheng, B. Gu, X. Liu, J. Kang, Q. Zhang, Y. Wang, Direct and highly selective conversion of synthesis gas to lower olefins: design of a bifunctional catalyst combining methanol synthesis and carbon-carbon coupling, *Angew. Chem. Int. Ed.* 55 (2016) 4725–4728, <https://doi.org/10.1002/ange.201601208>.
- [10] F. Jiao, X. Liu, K. Gong, Y. Chen, G. Li, X. Bao, Shape-Selective Zeolites Promote ethylene formation from syngas via a ketene intermediate, *Angew. Chem. Int. Ed.* 57 (2018) 4692–4696, <https://doi.org/10.1002/ange.200703335>.
- [11] Y. Cheng, J. Lin, T. Wu, H. Wang, S. Xie, Y. Pei, M. Qiao, B. Zong, Mg and K dual-decorated Fe-on-reduced graphene oxide for selective catalyzing CO hydrogenation to light olefins with mitigated CO<sub>2</sub> emission and enhanced activity, *Appl. Catal. B* 204 (2017) 475–485, <https://doi.org/10.1016/j.apcatb.2016.11.058>.
- [12] H.M. Torres Galvis, J.H. Bitter, T. Davidian, M. Ruitenbeek, A.I. Dugulan, K.P. de Jong, Iron particle size effects for direct production of lower olefins from synthesis gas, *J. Am. Chem. Soc.* 134 (2012) 16207–16215, <https://doi.org/10.1021/ja304958u>.
- [13] S. Sartipi, K. Parashar, M.J. Valero-Romero, V.P. Santos, B. Van Der Linden, M. Makkee, F. Kapteijn, J. Gascon, Hierarchical H-ZSM-5-supported cobalt for the direct synthesis of gasoline-range hydrocarbons from syngas: advantages, limitations, and mechanistic insight, *J. Catal.* 305 (2013) 179–190, <https://doi.org/10.1016/j.jcat.2013.05.012>.
- [14] H.M. Torres Galvis, J.H. Bitter, C.B. Khare, M. Ruitenbeek, A.I. Dugulan, K.P. de Jong, Supported iron nanoparticles as catalysts for sustainable production of lower olefins, *Science* 335 (2012) 835–838, <https://doi.org/10.1126/science.1215614>.
- [15] L. Zhong, F. Yu, Y. An, Y. Zhao, Y. Sun, Z. Li, T. Lin, Y. Lin, X. Qi, Y. Dai, Y. Gu, J. Hu, S. Jin, Q. Shen, H. Wang, Cobalt carbide nanoprisms for direct production of lower olefins from syngas, *Nature* 538 (2016) 84–87, <https://doi.org/10.1038/nature19786>.
- [16] F. Jiao, J. Li, X. Pan, J. Xiao, H. Li, H. Ma, M. Wei, Y. Pan, Z. Zhou, M. Li, S. Miao, J. Li, Y. Zhu, D. Xiao, T. He, J. Yang, F. Qi, Q. Fu, X. Bao, Selective conversion of syngas to light olefins, *Science* 351 (2016) 1065–1068, <https://doi.org/10.1126/science.aaf1835>.
- [17] Y. Xu, X. Li, J. Gao, J. Wang, G. Ma, X. Wen, Y. Yang, Y. Li, M. Ding, A hydrophobic FeMn@Si catalyst increases olefins from syngas by suppressing C1 by-products, *Science* 371 (2021) 610–613, <https://doi.org/10.1126/science.abb3649>.
- [18] J.P. Perdew, K. Burke, M. Ernzerhof, Generalized gradient approximation made simple, *Phys. Rev. Lett.* 77 (1996) 3865–3868, <https://doi.org/10.1103/PhysRevLett.77.3865>.
- [19] P.E. Blöchl, Projector augmented-wave method, *Phys. Rev. B* 50 (1994) 17953, <https://doi.org/10.1103/PhysRevB.50.17953>.
- [20] G. Kresse, J. Furthmüller, Efficient iterative schemes for ab initio total-energy calculations using a plane-wave basis set, *Phys. Rev. B* 54 (1996) 11169–11186, <https://doi.org/10.1103/PhysRevB.54.11169>.
- [21] G.L. Bezemer, J.H. Bitter, H.P. Kuipers, H. Oosterbeek, J.E. Holewijn, X. Xu, F. Kapteijn, A. Jos Van Dillen, K.P. de Jong, Cobalt particle size effects in the Fischer–Tropsch reaction studied with carbon nanofiber supported catalysts, *J. Am. Chem. Soc.* 128 (2006) 3956–3964, <https://doi.org/10.1021/ja058282w>.
- [22] T. Lin, F. Yu, Y. An, T. Qin, L. Li, K. Gong, L. Zhong, Y. Sun, Cobalt carbide nanocatalysts for efficient syngas conversion to value-added chemicals with high selectivity, *Acc. Chem. Res.* 54 (2021) 1961–1971, <https://doi.org/10.1021/acs.accounts.0c00883>.
- [23] Z. Li, L. Zhong, F. Yu, Y. An, Y. Dai, Y. Yang, T. Lin, S. Li, H. Wang, P. Gao, Y. Sun, M. He, Effects of sodium on the catalytic performance of CoMn catalysts for Fischer–Tropsch to olefin reactions, *ACS Catal.* 7 (2017) 3622–3631, <https://doi.org/10.1021/acscatal.6b03478>.
- [24] Y. An, Y. Zhao, F. Yu, T. Lin, Y. Lu, S. Li, Z. Li, Y. Dai, X. Wang, H. Wang, L. Zhong, Y. Sun, Morphology control of Co<sub>2</sub>C nanostructures via the reduction process for direct production of lower olefins from syngas, *J. Catal.* 366 (2018) 289–299, <https://doi.org/10.1016/j.jcat.2018.03.024>.
- [25] R. Yang, Z. Xia, Z. Zhao, F. Sun, X. Du, H. Yu, S. Gu, L. Zhong, J. Zhao, Y. Ding, Z. Jiang, Characterization of CoMn catalyst by *in situ* X-ray absorption spectroscopy and wavelet analysis for Fischer–Tropsch to olefins reaction, *J. Energy Chem.* 32 (2019) 118–123, <https://doi.org/10.1016/j.jechem.2018.07.005>.
- [26] F. Sun, R. Yang, Z. Xia, Y. Yang, Z. Zhao, S. Gu, D. Wu, Y. Ding, Z. Jiang, Effects of cobalt carbide on Fischer–Tropsch synthesis with MnO supported Co-based catalysts, *J. Energy Chem.* 42 (2020) 227–232, <https://doi.org/10.1016/j.jechem.2019.07.007>.
- [27] T. Ma, S. Dai, M. Jaroniec, S. Qiao, Metal–organic framework derived hybrid Co<sub>3</sub>O<sub>4</sub>–carbon porous nanowire arrays as reversible oxygen evolution electrodes, *J. Am. Chem. Soc.* 136 (2014) 13925–13931, <https://doi.org/10.1021/ja0582553>.
- [28] A. Ajaj, J. Masa, C. Rösler, W. Xia, P. Weide, A.J. Botz, R.A. Fischer, W. Schuhmann, M. Muhler, Co@Co<sub>3</sub>O<sub>4</sub> encapsulated in carbon nanotube-grafted nitrogen-doped carbon polyhedra as an advanced bifunctional oxygen electrode, *Angew. Chem. Int. Ed.* 55 (2016) 4087–4091, <https://doi.org/10.1002/anie.201509382>.
- [29] J. Xie, P.P. Paalanen, T.W. van Deelen, B.M. Weckhuysen, M.J. Louwerse, K.P. de Jong, Promoted cobalt metal catalysts suitable for the production of lower olefins from natural gas, *Nat. Commun.* 10 (2019) 167–176, <https://doi.org/10.1038/s41467-018-08019-7>.
- [30] L. Wang, E. Guan, Y. Wang, L. Wang, Z. Gong, Y. Cui, X. Meng, B.C. Gates, F. Xiao, Silica accelerates the selective hydrogenation of CO<sub>2</sub> to methanol on cobalt catalysts, *Nat. Commun.* 11 (2020) 1033–1041, <https://doi.org/10.1038/s41467-020-14817-9>.
- [31] J.G. Chen, Carbide and nitride overlayers on early transition metal surfaces: preparation, characterization, and reactivities, *Chem. Rev.* 4 (1996) 1477–1498, <https://doi.org/10.1021/cr950232u>.
- [32] M.R. Wang, P. Wang, G.H. Zhang, Y.L. Liu, R.T. Li, J. Zhu, J.Y. Wang, K. Bian, Y. Liu, F.S. Ding, T.P. Senthil, Q. Fu, C.S. Song, X.W. Guo, In situ synthesis and stabilization of Co<sub>2</sub>C for CO<sub>2</sub> hydrogenation to valuable hydrocarbon. Available at SSRN 4186997.
- [33] P. Chen, J. Liu, W. Li, Carbon monoxide activation on cobalt carbide for Fischer–Tropsch synthesis from First-Principles theory, *ACS Catal.* 9 (2019) 8093–8103, <https://doi.org/10.1021/acscatal.9b00649>.
- [34] C.J. Weststrate, D. Sharma, D.G. Rodriguez, M.A. Gleeson, H.O. Fredriksson, J. W. Niemantsverdriet, Mechanistic insight into carbon–carbon bond formation on cobalt under simulated Fischer–Tropsch synthesis conditions, *Nat. Commun.* 11 (2020) 750–759, <https://doi.org/10.1038/s41467-020-14613-5>.
- [35] R.A. van Santen, M.M. Ghouri, S. Shetty, E.M. Hensen, Structure sensitivity of the Fischer–Tropsch reaction: molecular kinetics simulations, *Catal. Sci. Technol.* 1 (2011) 891–911, <https://doi.org/10.1039/C1CY00118C>.
- [36] P. van Helden, I.M. Ciobăcă, R.L. Coetzer, The size-dependent site composition of FCC cobalt nanocrystals, *Catal. Today* 261 (2016) 48–59, <https://doi.org/10.1016/j.cattod.2015.07.052>.

[37] J.P. Den Breejen, P.B. Radstake, G.L. Bezemer, J.H. Bitter, V. Frøseth, A. Holmen, K.P. de Jong, On the origin of the cobalt particle size effects in Fischer–Tropsch catalysis, *J. Am. Chem. Soc.* 131 (2009) 7197–7203, <https://doi.org/10.1021/ja901006x>.

[38] M.C. Biesinger, B.P. Payne, A.P. Grosvenor, L.W. Lau, A.R. Gerson, R.S.C. Smart, Resolving surface chemical states in XPS analysis of first row transition metals, oxides and hydroxides: Cr, Mn, Fe, Co and Ni, *Appl. Surf. Sci.* 257 (2011) 2717–2730, <https://doi.org/10.1016/j.apsusc.2010.10.051>.

[39] E.S. Ilton, J.E. Post, P.J. Heaney, F.T. Ling, S.N. Kerisit, XPS determination of Mn oxidation states in Mn (hydr) oxides, *Appl. Surf. Sci.* 366 (2016) 475–485, <https://doi.org/10.1016/j.apsusc.2015.12.159>.

[40] G.R. Johnson, S. Werner, A.T. Bell, An investigation into the effects of Mn promotion on the activity and selectivity of Co/SiO<sub>2</sub> for Fischer-Tropsch synthesis: evidence for enhanced CO adsorption and dissociation, *ACS Catal.* 5 (2015) 5888–5903, <https://doi.org/10.1021/acscatal.5b01578>.